

---

## Oceanic control of multidecadal variability in an idealized coupled GCM

Jamet Quentin <sup>1,\*</sup>, Huck Thierry <sup>3</sup>, Arzel Olivier <sup>1</sup>, Campin Jean-Michel <sup>2</sup>, Colin De Verdiere Alain <sup>1</sup>

<sup>1</sup> Laboratoire de Physique des Océans (UMR 6523 CNRS IFREMER IRD UBO), Université de Bretagne Occidentale, UFR Sciences, 6 avenue Le Gorgeu, CS 93837, 29238, Brest Cedex 3, France

<sup>2</sup> Department of Earth, Atmospheric and Planetary Sciences, Massachusetts Institute of Technology, 77 Massachusetts Ave, Cambridge, MA, 02139, USA

\* Corresponding author : Quentin Jamet, email address : [quentin.jamet@univ-brest.fr](mailto:quentin.jamet@univ-brest.fr)

---

### Abstract :

Idealized ocean models are known to develop intrinsic multidecadal oscillations of the meridional overturning circulation (MOC). Here we explore the role of ocean–atmosphere interactions on this low-frequency variability. We use a coupled ocean–atmosphere model set up in a flat-bottom aquaplanet geometry with two meridional boundaries. The model is run at three different horizontal resolutions (4°, 2° and 1°) in both the ocean and atmosphere. At all resolutions, the MOC exhibits spontaneous variability on multidecadal timescales in the range 30–40 years, associated with the propagation of large-scale baroclinic Rossby waves across the Atlantic-like basin. The unstable region of growth of these waves through the long wave limit of baroclinic instability shifts from the eastern boundary at coarse resolution to the western boundary at higher resolution. Increasing the horizontal resolution enhances both intrinsic atmospheric variability and ocean–atmosphere interactions. In particular, the simulated atmospheric annular mode becomes significantly correlated to the MOC variability at 1° resolution. An ocean-only simulation conducted for this specific case underscores the disruptive but not essential influence of air–sea interactions on the low-frequency variability. This study demonstrates that an atmospheric annular mode leading MOC changes by about 2 years (as found at 1° resolution) does not imply that the low-frequency variability originates from air–sea interactions.

**Keywords :** Atlantic multidecadal oscillation, Air– sea interactions, NAO, Rossby waves, Idealized configuration

### 1 Introduction

---

The Atlantic Multidecadal Oscillation (AMO, Kerr, 2000) is a significant mode of natural variability (Delworth et al, 2007) seen in averaged Sea Surface Temperature (SST) over the North Atlantic. The AMO has a well-established impact on climatic conditions over Europe, North America and Africa (Folland et al, 1986; Enfield et al, 2001; Sutton and Hodson, 2005). Early studies describe the AMO as a mode of variability with a 50-70 yr period (Enfield et al, 2001; Knight et al, 2005), but more recent studies also highlight another mode of variability with a period of about 20-30 yr (Frankcombe et al, 2008; Frankcombe and Dijkstra, 2009; Chylek et al, 2011).

37 The Meridional Overturning Circulation (MOC) in the Atlantic transports  
38 warm water northward at the surface and colder water southward at depth, re-  
39 sulting in a net northward heat transport. Changes in MOC heat transport are  
40 thought to modulate North Atlantic SST on multidecadal timescales, thereby the  
41 AMO (Schlesinger and Ramankutty, 1994; Kushnir, 1994). Delworth et al (1993)  
42 have shown the existence of a multidecadal Atlantic MOC variability using the  
43 GFDL coupled model, and Knight et al (2005) linked this MOC variability to the  
44 surface SST anomalies defining the AMO.

45 There is still no consensus on the mechanism that generates this multidecadal  
46 climate variability in the North Atlantic, particularly regarding the role of the at-  
47 mosphere (Liu, 2012). Several hypotheses have been proposed which include either  
48 ocean-atmosphere coupled modes (Timmermann et al, 1998; Weaver and Valcke,  
49 1998), oceanic modes that are excited by atmospheric noise associated with synop-  
50 tic weather (Griffies and Tziperman, 1995; Sévellec et al, 2009; Frankcombe et al,  
51 2009), oceanic response to variable atmospheric forcing (Delworth and Greatbatch,  
52 2000; Eden and Jung, 2001; Eden and Willebrand, 2001), or intrinsic oceanic modes  
53 where the energy source originates from an internal instability of the large-scale  
54 ocean circulation (Colin de Verdière and Huck, 1999; Te Raa and Dijkstra, 2002).

55 The progress in understanding the behaviour of the Atlantic ocean circulation  
56 on multidecadal timescales has largely benefited from studies based on models  
57 forced at the surface by either synthetic or observed fluxes of heat, freshwater and  
58 momentum. The idea that the North Atlantic Oscillation (NAO, Hurrell, 1995)  
59 forcing is the main driver of Atlantic multidecadal variability was thus explored  
60 in a number of studies (e.g. Eden and Jung, 2001; Eden and Willebrand, 2001;  
61 Mecking et al, 2014). Although the processes and timescales involved in the oceanic

62 response may depend on both the exact nature of the forcings and the model  
63 configuration, the conclusion was reached that the NAO forcing is essential to  
64 the oceanic multidecadal variability and to reproduce part of the observed North  
65 Atlantic SST signal.

66 By contrast, when forced by fixed surface fluxes, idealized flat bottom ocean-  
67 only models have revealed their potential to generate multidecadal MOC oscilla-  
68 tions (Colin de Verdière and Huck, 1999; Te Raa and Dijkstra, 2002). This intrinsic  
69 variability is associated with westward propagating Rossby waves, sustained  
70 through large-scale baroclinic instability. This mechanism has been shown to be  
71 robust to the coupling to a variety of idealized atmospheric models, like energy  
72 balance models (Fanning and Weaver, 1998; Huck et al, 2001) or zonally-averaged  
73 statistical-dynamical atmosphere (Arzel et al, 2007). This variability was also identified  
74 in realistic geometry ocean models, forced by fixed surface fluxes (Sévellec  
75 and Fedorov, 2013), or coupled to an atmospheric energy balance model (Arzel  
76 et al, 2012), but with a damped character due to a variety of processes. Intro-  
77 ducing a 3D dynamical atmosphere, Buckley et al (2012) recently explored the  
78 multidecadal variability arising in two coupled model configurations with sim-  
79 plified flat bottom and bowl oceanic geometry. They highlighted the key role of  
80 unstable westward propagating Rossby waves in sustaining the oceanic variability.  
81 In flat bottom configuration, stochastic atmospheric variability was shown to be  
82 unnecessary to the existence of the variability. When the flat bottom approxima-  
83 tion is relaxed, and idealized (Winton, 1997) or realistic (Sévellec and Fedorov,  
84 2013) bottom topography added to the ocean model, the intrinsic oceanic variabil-  
85 ity may require an extra source of energy to be maintained. The atmosphere is a  
86 potential candidate to energize the oceanic variability, as shown in many studies

87 (e.g. Delworth and Greatbatch, 2000; Frankcombe and Dijkstra, 2009; Buckley  
88 et al, 2012).

89 Our study builds upon the work of Buckley et al (2012). The objective is to  
90 find out whether the intrinsic oceanic nature of the variability simulated by their  
91 flat bottom coupled model is modified when the horizontal resolution increases si-  
92 multaneously in both the ocean and the atmosphere from  $4^\circ$  to  $1^\circ$ . Increasing the  
93 horizontal resolution has the potential to increase the intrinsic atmospheric vari-  
94 ability and the atmospheric response to changes in ocean circulation (Hodson and  
95 Sutton, 2012), through an improved representation of transient eddy fluxes (see  
96 the review by Kushnir et al, 2002). Both processes can contribute to increase the  
97 role of the atmosphere in the low-frequency climate variability. Such resolutions  
98 remain beyond the scale required to resolve oceanic eddies, but mesoscale turbu-  
99 lence is though to have a minor impact on the existence of multidecadal oceanic  
100 variability (Penduff et al, 2011; Huck et al, 2015). The aim of this study is rather  
101 to shed light on the mechanisms of multidecadal variability in a North Atlantic-  
102 like ocean at low resolution. The Double Drake configuration of the MIT General  
103 Circulation Model (Ferreira et al, 2010; Marshall et al, 1997) used by Buckley et al  
104 (2012) is the starting point of our study. The focus is placed upon the influence of  
105 the atmospheric dynamics on the low frequency oceanic variability. Because the  
106 latter is affected by the presence of variable topography (Winton, 1997; Buckley  
107 et al, 2012), this study is carried out using only a flat bottom ocean configuration  
108 as a first step.

109 This paper is organized as follows. The coupled model is described in section  
110 2, as well as the ocean and atmosphere climatological mean states of the three  
111 configurations with horizontal resolution of  $4^\circ$ ,  $2^\circ$  and  $1^\circ$ . In section 3, we show

112 that the MOC is dominated by a 30-40 yr variability in all 3 set-ups, related to  
113 the propagation of large-scale Rossby waves. Density (dominated by temperature)  
114 anomalies propagate from east to west across the subpolar gyre, interacting with  
115 the MOC along the western boundary. At  $1^\circ$  resolution, the signal is less regular  
116 with more energy at high frequency. In section 4, the respective role of internal  
117 ocean dynamics and air-sea **interactions** in explaining the low-frequency oceanic  
118 variability is disentangled through the use of a linearized temperature variance  
119 equation, **and an ocean-only experiment**. In section 5, we finally summarize  
120 and discuss our results.

## 121 **2 Description of the model and mean states**

### 122 2.1 Numerical characteristics

123 We use the ocean-atmosphere-sea ice coupled MITgcm - Massachusetts Institute  
124 of Technology general circulation model (Marshall et al, 1997) - in the Double  
125 Drake configuration (Ferreira et al, 2010). The flat-bottom 3 km depth ocean  
126 has 15 vertical levels, with thickness increasing from 30 m at the surface to 400  
127 m at the bottom, and two meridional barriers extended from the north pole to  
128  $34^\circ\text{S}$  represented as physical walls of about 400 km width for the ocean. These  
129 continental barriers divide the ocean in a small, a large and an unblocked southern  
130 circumpolar basin, each of them aiming at crudely representing the Atlantic, the  
131 Indo-Pacific and the Southern ocean basin, respectively. The small basin is the  
132 site of a deep convection and deep overturning cell, referred to as the MOC in  
133 the following. The impacts of unresolved eddies are parametrized as an advective  
134 process (Gent and McWilliams, 1990) and an isopycnal diffusion (Redi, 1982) with

135 a transfer coefficient of  $1200 \text{ m}^2\text{s}^{-1}$  for both processes, in the range of observed  
136 values (Ollitrault and Colin de Verdière, 2002). Enhanced vertical mixing ( $100$   
137  $\text{m}^2\text{s}^{-1}$ ) of temperature and salinity applies whenever static instability occurs. The  
138 background vertical diffusivity is uniform and set to  $3 \times 10^{-5} \text{ m}^2\text{s}^{-1}$ . These mixing  
139 coefficients are identical to those used by Ferreira et al (2010).

140 The atmospheric physics is based on the Simplified Parametrization, Primi-  
141 tive Equation Dynamics (SPEEDY, Molteni, 2003). It is a spectral model com-  
142 posed of 5 vertical levels. The parametrisations incorporated within the model are  
143 large-scale condensation, convection, diagnostic clouds, short-wave and long-wave  
144 radiation, surface fluxes and vertical diffusion.

145 Both oceanic and atmospheric models are integrated forward on the same  
146 cubed-sphere horizontal grid (Adcroft et al, 2004). This idealised coupled model  
147 is run in three configurations with increasing horizontal resolution. For the origi-  
148 nal set-up, each face of the cube has  $24 \times 24$  grid points, leading to an horizontal  
149 resolution of about  $4^\circ$ . This set-up is referred to as cs24 hereafter (cs stands for  
150 Cubed-Sphere). This barely resolves the typical scale of synoptic atmospheric per-  
151 turbations. The initial horizontal resolution of both ocean and atmosphere models  
152 is increased to cube faces divided in  $48 \times 48$  and  $96 \times 96$  horizontal grid points, re-  
153 sulting in horizontal resolution of about  $2^\circ$  and  $1^\circ$ , respectively (hereafter cs48  
154 and cs96). The zonal extent of the land barriers is kept constant and roughly  
155 equal to 400 km. As the horizontal resolution of the dynamical core is increased,  
156 oceanic eddy lateral viscosity is reduced; the other physical parametrizations are  
157 unchanged. In particular vertical viscosity and turbulent diffusivities of oceanic  
158 eddies are kept constant. The main computational characteristics of the three  
159 configurations are summarized in table 1.

160 All three set-ups are initialised from the equilibrated oceanic state obtained by  
161 Ferreira et al (2010). Tracer fields (temperature  $T$  and salinity  $S$ ) are interpolated  
162 to fit the new grids of cs48 and cs96. Atmospheric initial conditions for all 3  
163 configurations are horizontally uniform and vertically stratified, and the model is  
164 initially free of ice. Under such initial conditions, both cs24 and cs48 quickly adjust,  
165 reaching equilibrium after less than 100 yr of integration, whereas cs96 requires  
166 more than 300 yr to reach equilibrium. During this 300 yr adjustment, the global  
167 mean oceanic temperature in cs96 decreases by about 0.6 K, and then slowly  
168 drifts by about 0.03 K/century. In both cs24 and cs48, the trend in temperature  
169 is smaller than 0.005 K/century. All set-ups are integrated forward in time for 600  
170 yr. To analyse the longest time series and avoid adjustment period, we perform  
171 analyses on the last 400 yr. Mean state of cs48 and cs96 are first compared to the  
172 well documented mean state of cs24 (Ferreira et al, 2010; Buckley et al, 2012).

## 173 2.2 Atmospheric mean state

174 The zonal mean atmosphere is composed of two active baroclinic regions at mid-  
175 latitudes (Fig. 1), with westward jet streams reaching  $40 \text{ m s}^{-1}$  at 250 mb in cs24.  
176 Increasing the resolution has two main consequences for the atmosphere: eddy-  
177 driven jets shift poleward, and their amplitude weakens. The first consequence is  
178 common to many atmospheric models (Pope and Stratton, 2002; Arakelian and  
179 Codron, 2012). This poleward shift brings atmospheric model in better agreement  
180 with observations, revealing the necessity of a sufficiently high resolution to cor-  
181 rectly represent a realistic climate. It is interesting to note that our idealized model  
182 reproduces a similar behaviour, highlighting its relatively high skills in simulat-

183 ing the mean state of the global climate. The weakening of the eddy-driven jets  
184 is associated with their widening, in agreement with Harnik and Chang (2004).  
185 As expected, the storm-tracks, computed as the standard deviation of daily Sea  
186 Level Pressure Anomaly (SLPA), strongly increase with the resolution (Pope and  
187 Stratton, 2002). The more vigorous storm-tracks are associated with an increased  
188 low frequency atmospheric variability (see section 4.1 for details).

189 For all set-ups, the poleward Atmospheric Heat Transport (AHT) is similar,  
190 peaking at about 4.5 PW (5-6 PW) at 40°N (40°S), in agreement with observa-  
191 tions (Trenberth et al, 2001). The slight enhancement of AHT in the southern  
192 hemisphere is attributed to a more vigorous storm-track in this region (Ferreira  
193 et al, 2010), a north-south asymmetry observed at all resolutions. The mid-latitude  
194 AHT is almost entirely achieved by the eddy contribution at all resolutions, while  
195 the time mean circulation contributes only in the tropics.

### 196 2.3 Oceanic mean state

197 The realistic wind-stress forcing over the small basin (Fig. 1, bottom right panel)  
198 drives a barotropic circulation (Fig. 2, upper panels) composed of a weak tropical  
199 cyclonic gyre ( $\sim 10$  Sv,  $1 \text{ Sv} = 10^6 \text{ m}^3\text{s}^{-1}$ ), a subtropical anticyclonic gyre ( $\sim 30$   
200 Sv) and a subpolar cyclonic gyre ( $\sim 25$  Sv). Following the poleward shift of the  
201 atmospheric jets, the position of the zero wind-stress curl line is displaced north-  
202 ward in the Northern Hemisphere with the increasing resolution. The intergyre  
203 position is displaced northward, and the subpolar cyclonic gyre in cs96 extends up  
204 to 70°N with a weak intensification along the western boundary. Due to weaker



205 polar easterlies in cs48 and cs96 (Fig. 1), the weak anticyclonic gyre ( $\sim 2$  Sv)  
206 present in cs24 north of  $60^\circ\text{N}$  disappears at higher resolution.

207       Increasing the horizontal resolution also strengthens the mean MOC maximum  
208 in the small basin from about 25 Sv in cs24 to about 30 Sv in cs96 (Fig. 2, bottom  
209 panels). Marsh et al (2009) observed a similar MOC strengthening in the OCCAM  
210 ocean model when the resolution is refined from  $1/4^\circ$  to  $1/12^\circ$ , but they mainly  
211 attributed this difference to the effect of resolved eddies. Here, the stronger MOC  
212 in cs96 is attributed to an increase of surface density resulting from increased heat  
213 losses and freshwater export over the northern small basin. North of  $45^\circ\text{N}$ , the  
214 zonally averaged oceanic heat loss over the small basin is about 20% ( $10 \text{ W m}^{-2}$ )  
215 stronger in cs96 compared to cs24. In addition, Ferreira et al (2010) show that  
216 the small basin of the Double Drake model is characterized by a deep overturning  
217 cell due to the excess of net evaporation (evaporation minus precipitation, E-  
218 P) within this basin. This E-P excess is sensitive to horizontal resolution, with a  
219 significant enhancement north of  $40^\circ\text{N}$ , mainly due to increased evaporation within  
220 the small basin rather than reduced precipitation. This results in a more vigorous  
221 salinification of the small basin, and an enhanced MOC.

### 222 **3 Oceanic multidecadal variability**

223 We now focus our attention on the multidecadal oceanic variability in the small  
224 basin. At coarse resolution (cs24), Buckley et al (2012) have shown that the MOC  
225 undergoes a variability on multidecadal timescales. In their flat bottom configura-  
226 tion, the variability is described as an ocean-only mode damped by air-sea heat  
227 fluxes, with a red spectrum and a strong peak at a period of about 34 yr. In this

228 section, we investigate the robustness of the MOC multidecadal variability with  
229 respect to increased atmospheric and oceanic resolution, and the accompanying  
230 increase in atmospheric variability.

### 231 3.1 MOC variability

232 We use the MOC index defined by Buckley et al (2012) as the average of the small  
233 basin MOC in the box [8°-60°N, 460-1890 m depth] (black box in Fig. 2, bottom  
234 panels). Specifically, the yearly time series of the maximum MOC is computed at  
235 each latitude within the box, and then averaged across the range of latitude. To  
236 assess the coherence of this index, we compare it to 8 other time series related to  
237 the overturning (Table 2). Correlations between the initial index and the resulting  
238 time series are high ( $r \geq 0.80$ ) except for the MOC at 63°N. These high correla-  
239 tions highlight the coherence of the MOC variability over the domain, and give  
240 confidence in the use of Buckley et al (2012) index at all three resolutions. This  
241 yearly index is computed over the last 400 yr of simulations (Fig. 3, left panel).  
242 It is used in the following as an indicator of the oceanic low-frequency variabil-  
243 ity. All analyses are performed with yearly outputs. However, results are weakly  
244 sensitive to the application of a 10-yr running mean. The MOC index presents a  
245 weak amplitude signal at multi-centennial timescales in cs96, with a weak positive  
246 (negative) trend between years 200-400 (400-600). The shortness of the model in-  
247 tegration does not allow us to conclude whether this is an intrinsic oscillation or  
248 due to the longer adjustment of this set-up.

249 At all resolutions, the MOC undergoes a variability on multidecadal timescales,  
250 with an **increased amplitude** for cs48 and cs96 compared to cs24, and a noisier

251 variability for cs96. The power spectrum analysis of the yearly index reveals a  
 252 dominant period of 32 yr for both cs24 and cs96, and 43 yr for cs48 (Fig. 3, right  
 253 panel), consistent with time scales usually found in both models and observations  
 254 (Frankcombe and Dijkstra, 2009; Frankcombe et al, 2010). The most important  
 255 difference is the less regular MOC variations for cs96. We will show in section 4 that  
 256 this difference mainly results from a stronger impact of atmospheric variability on  
 257 the ocean circulation.

258 The western boundary has been shown to be a key region to monitor the MOC  
 259 variability (Hirschi and Marotzke, 2007; Tulloch and Marshall, 2012; Buckley et al,  
 260 2012). Those studies relate the MOC variability to the east-west boundary density  
 261 difference through the thermal wind relationship (see Appendix 2). Following their  
 262 work, we reconstruct the variability of the MOC index by computing the zonally  
 263 integrated geostrophic meridional velocity resulting from the difference between  
 264 density anomalies along the eastern and the western boundary (Eq. (4) in Ap-  
 265 pendix 2). The resulting meridional velocities are vertically integrated to obtain  
 266 the reconstructed MOC anomaly  $\psi_{\rho}^*$  (Eq. (5), Fig. 4 red curves). The MOC index  
 267 computed from  $\psi_{\rho}^*$  is compared to the model MOC index by computing the skill  $S$   
 268 between these two time series (Eq. (8)). The skill for the reconstructed MOC index  
 269 is 0.78 (0.93, 0.94) for cs24 (cs48, cs96, respectively). These good skills highlight  
 270 the dominant contribution of the geostrophic shear for the MOC variations (the  
 271 Ekman shear plays a minor role and the contribution of the barotropic mode is  
 272 strictly zero due to flat bottom).

273 We can go a step further in the approximation by considering only tempera-  
 274 ture anomalies along the western boundary in Eq. (7) ( $\psi_{T_w}^*$ , Fig. 4, blue curves).  
 275 The matching between the model and  $\psi_{T_w}^*$  MOC indices is striking, revealing

276 the key role of the western boundary temperature anomalies in explaining MOC  
277 variations. In cs96 however, both indices present a trend (black and blue dashed  
278 lines on Fig. 4, right panel), probably due to the longer adjustment of this set-  
279 up (see section 2.1). To solely keep the decadal variations in computing the skill  
280 between the reconstructed MOC index and the model MOC index, these trends  
281 have been preliminary removed. By only considering temperature anomalies along  
282 the western boundary, the skill reduces to  $S = 0.15$  (0.46, 0.58) for cs24 (cs48,  
283 cs96, respectively). These low skills mainly reflect the lag of few years between  
284 the model and  $\psi_{T_w}^*$  MOC indices, (**Fig. 4, black and blue curves respectively**).  
285 **However the 2 time series are relatively well correlated with  $r = 0.66$  (0.82,**  
286 **0.78) for cs24 (cs48, cs96, respectively). When the lag is removed and both**  
287 **time series are in phase, the correlation reaches  $r = 0.79$  (0.90, 0.84).**

288 **Analysis of  $\psi_{T_w}^*$  demonstrates that the MOC variability in all set-ups**  
289 **is mainly geostrophic, driven by temperature anomalies along the western**  
290 **boundary. These anomalies can be tracked along the western boundary**  
291 **to understand MOC variability (Fig. 5).** Negative temperature anomalies on  
292 the western boundary, with a subsurface intensification between  $40^\circ$ - $60^\circ$ N, are  
293 associated with positive MOC anomalies. They strike the western boundary few  
294 years before a MOC minimum, travel southward and downward following the mean  
295 isotherms, and lead to MOC anomalies further south (not shown).

### 296 3.2 Associated temperature anomalies

297 The small basin is characterized by large scale, depth coherent, temperature anoma-  
298 lies that covary with the MOC index. To illustrate this, yearly potential temper-

299 ature anomalies averaged over the 1000 m upper ocean (referred to as T1000  
300 further) associated with one standard deviation of the MOC index with different  
301 phase lags are shown on Fig. 6 (see caption for details). Prior a MOC maximum,  
302 positive T1000 anomalies appear and grow along the eastern boundary, and spread  
303 almost all over the subpolar gyre after a MOC maximum. Negative anomalies expe-  
304 rience the same dynamics around a minimum of MOC. The horizontal signature of  
305 large-scale T1000 anomalies is harder to track in cs96, with more complex patterns  
306 (Fig. 6, bottom row panels). We still observe negative (positive) T1000 anomalies  
307 within the subpolar gyre prior (after) a MOC maximum, but the region of growth  
308 along the eastern boundary observed at coarser resolution is no longer significant.

309 Large-scale baroclinic instability has been proposed for sustaining these per-  
310 turbations (Colin de Verdière and Huck, 1999). This mechanism is principally  
311 identified through the vertical structure of temperature anomalies, and the asso-  
312 ciated meridional eddy heat fluxes (the latter will be discussed in section 4.2.1).  
313 The vertical structure of temperature anomalies is computed within the region of  
314 highest standard deviation of T1000, between  $60^{\circ}$ - $70^{\circ}$ N, near the eastern bound-  
315 ary. Temperature anomalies are intensified at sub-surface, with a maximum at 265  
316 m depth for cs24 and at 540 m depth for both cs48 and cs96, highlighting their  
317 surface damping by turbulent atmospheric fluxes. They exhibit a vertical tilt, with  
318 sub-surface anomalies leading deep anomalies with a quarter phase lag, in agree-  
319 ment with classical theory (Colin de Verdière and Huck, 1999; Sévellec and Huck,  
320 2015).

321 To illustrate the westward propagation across the basin, longitude-time (Hovmöller)  
322 diagrams have been computed at various latitudes. It appears that  $60^{\circ}$ N,  $65^{\circ}$ N and  
323  $70^{\circ}$ N are the most relevant ones to capture the propagating signal for cs24, cs48

324 and cs96, respectively. It is interesting to note that these specific latitudes also  
325 roughly correspond to the zero-wind stress curl line associated with large scale  
326 wind distribution described in section 2.2. Hovmöller diagrams computed at these  
327 latitudes (Fig. 7), show a westward propagation of temperature anomalies, with  
328 an estimated phase velocity of about  $0.40 \text{ cm s}^{-1}$  for all experiments. They prop-  
329 agate slower in the eastern half of the small basin ( $0.36$ ,  $0.26$  and  $0.21 \text{ cm s}^{-1}$  for  
330 cs24, cs48 and cs96, respectively) than in the western half ( $0.83$ ,  $0.70$  and  $0.74 \text{ cm}$   
331  $\text{s}^{-1}$ ), as estimated from the slope of the white lines in Fig. 7. The phase speed of  
332 baroclinic modes computed from the mean stratification in the quasigeostrophic  
333 approximation (Huck et al, 2001, section 2c) does not explain such a speed-up in  
334 the western region. Taking into account the advection of anomalies by the mean  
335 barotropic flow (Doppler shift) qualitatively explains the observed acceleration  
336 westward, but underestimates the phase velocity. Incorporating the vertical shear  
337 of the mean flow within the baroclinic mode computation clearly improves the  
338 results: A detailed analysis is underway and will be reported in a dedicated study.

339 We now look at SST signature associated with the MOC variability because of  
340 its critical role for ocean-atmosphere interactions. Fig. 8 illustrates SST anoma-  
341 lies associated with one standard deviation of the MOC index (non-significant  
342 regressions are grey shaded). In all set-ups, these SST anomalies account for more  
343 than 50% of the total SST variability, but their global structures are very different  
344 between cs48/cs96 and cs24. For cs24, it is closely related to the propagation of  
345 large-scale temperature anomalies described in section 3.2. They emanate near the  
346 eastern boundary and propagate westward around  $60^\circ\text{N}$ . In cs48, positive anoma-  
347 lies are observed in two different regions: one along the eastern boundary, north  
348 of  $60^\circ\text{N}$ , and one along the western boundary in the subpolar gyre. The first one

349 is the surface signature of Rossby waves, propagating from east to west, while the  
350 second seems to be stationary. As the first one propagates toward the west, it  
351 slowly merges with the second one.

352 In both cs48 and cs96, SST are dominated by a widespread positive anomaly  
353 that covers the entire subpolar gyre, as observed in many other models (Danaba-  
354 soglu, 2008; Zhang, 2010; Tulloch and Marshall, 2012) and observations (Knight  
355 et al, 2005). Such a pattern is usually referred to as the Atlantic Multidecadal  
356 Oscillation (AMO) (Kerr, 2000; Enfield et al, 2001). The warming of the subpolar  
357 gyre induced by a strengthening of the MOC is usually attributed to a more vig-  
358 orous Oceanic Heat Transport (OHT) (Knight et al, 2005; Zhang, 2008). In our  
359 model, OHT anomalies associated with one standard deviation of the MOC index  
360 peak at about 0.03 PW (0.08, 0.06) at the subtropical-subpolar intergyre position  
361 for cs24 (cs48, cs96, respectively). They account for more than 65% of the OHT  
362 variability at this latitude. **While these OHT anomalies are significantly larger**  
363 **in cs48 and cs96, the regression coefficients between OHT and the MOC**  
364 **index are similar for all set-ups, such that larger OHT anomalies observed**  
365 **in cs48 and cs96 mainly result from a stronger MOC variability. They are**  
366 **mainly driven by the zonally integrated circulation (the MOC) in the sub-**  
367 **tropical gyre and by the gyre circulation (computed as the residual) in the**  
368 **subpolar gyre, and the partition between MOC and gyre OHT anomalies**  
369 **is relatively similar for all set-ups.** Through OHT anomalies, larger (positive)  
370 MOC anomalies in cs48 and cs96 induce positive SST anomalies within the subpo-  
371 lar gyre, as observed in Fig. 8. This advective process (OHT) conceals the surface  
372 signature of large scale baroclinic Rossby waves in cs48 and cs96. By contrast, the  
373 weaker OHT anomalies in cs24 induce weaker SST anomalies, allowing a much

374 clearer surface signature of such waves. The main idea to keep in mind is that  
375 SST anomalies that covary with the MOC (Fig. 8) present a different signature  
376 between cs24 and cs48/cs96, that can result in/from different air-sea interactions.  
377 This is what we aim to analyse in the following.

#### 378 **4 Role of atmospheric forcing and ocean dynamics**

379 We have shown that the MOC undergoes a similar variability in all set-ups, related  
380 to the propagation of large-scale baroclinic Rossby waves. At increasing horizontal  
381 resolution, the SST variability is different between cs24 and cs48/cs96, especially  
382 along the western boundary. This may have important implications for air-sea  
383 interactions. In this section, we aim to disentangle the respective role of internal  
384 ocean dynamics and air-sea interactions in explaining the low-frequency oceanic  
385 variability.

##### 386 **4.1 Atmospheric variability**

387 To help the discussion on the role of the atmospheric forcing for the low-frequency  
388 oceanic variability, we first focus on the internal atmospheric variability. **It is tra-**  
389 **ditionally diagnosed with the use of the first EOF of Sea Level Pressure**  
390 **Anomaly (SLPA) in the North Atlantic or the northern hemisphere, and**  
391 **referred to as the North Atlantic Oscillation (NAO, Hurrell, 1995) or the**  
392 **Northern Annular-Mode (NAM, Thompson and Wallace, 2001). Both pro-**  
393 **cesses result from internal atmospheric dynamics (Vallis et al, 2004, and**  
394 **references therein). The zonal asymmetry of the NAM/NAO is principally**  
395 **induced by land-sea contrasts (Thompson and Wallace, 1998), and the ab-**



396 **sence of realistic continents in our model favours the emergence of the NAM**  
397 **rather than the NAO. Because both NAM and NAO indices are highly cor-**  
398 **related (Deser, 2000), the NAM is used in the following in a similar manner**  
399 **as realistic model studies use the NAO.**

400 **In our model, the first EOF of the yearly SLPA explains about 60%**  
401 **of the variance in all set-ups, with a slight enhancement at increasing res-**  
402 **olution (Fig. 9). Its spatial structure is zonally uniform, with anomalies**  
403 **of opposite sign north/south of 60°N. Because this pattern resembles the**  
404 **NAM, it is referred to as such hereafter.** The amplitude of the atmospheric  
405 variability associated with the first EOF/PC (i.e. the NAM index) is computed  
406 with the absolute maximum of the spatial EOF1 pattern obtained with a projec-  
407 tion onto the standardized PC1 (Table 1). We observe a strong enhancement of  
408 the intrinsic atmospheric variability with increasing horizontal resolution, with a  
409 NAM amplitude that almost doubles from cs24 to cs96. The NAM variability is in-  
410 creased for all time scales, revealing a white spectrum of the atmosphere variability  
411 at low frequencies.

412 To estimate the impact of the enhanced atmospheric variability on the oceanic  
413 low frequency oscillation, we compute the correlation between the yearly SLPA in  
414 the northern hemisphere and the yearly MOC index. Using a statistical significance  
415 test based on a Monte Carlo approach (see Appendix 1), the most significant cor-  
416 relations are found when the SLPA leads the MOC by 2 yr in all set-ups (Fig. 10).  
417 At this lag, the correlation is significant only near the small basin northern corner  
418 and in the tropics for cs48, whereas for cs24 **almost no** significant correlations  
419 are obtained. This reveals the weak interaction between the oceanic and the at-  
420 mospheric variability at those resolutions. By contrast, a much more important

421 fraction of the SLPA is significantly correlated to the MOC variability in cs96,  
 422 with negative (positive) correlations northward (southward) of 60°N. This pat-  
 423 tern strongly resembles the NAM described above. By increasing the horizontal  
 424 resolution up to 1°, the intrinsic atmospheric variability is enhanced and becomes  
 425 significantly correlated to the MOC variability in cs96, with the NAM that leads  
 426 by 2 years the MOC variability. This feature is common to many other numerical  
 427 studies (Eden and Jung, 2001; Deshayes and Frankignoul, 2008; Gastineau and  
 428 Frankignoul, 2012), with a positive phase of the NAO that leads a maximum of  
 429 MOC by few years. They describe the MOC variability in the North Atlantic as an  
 430 oceanic response to stochastic atmospheric forcing. More recently, McCarthy et al  
 431 (2015) have shown that the observed NAO leads by 2-3 years their sea-level index,  
 432 a proxy for the ocean circulation at the intergyre position. Regarding these results,  
 433 we therefore ask the following question: Does the oceanic mode of variability re-  
 434 produced in our idealized model switch from an intrinsic oceanic mode at coarse  
 435 resolution (cs24), as shown by Buckley et al (2012), to an oceanic mode forced by  
 436 the atmosphere at higher resolution (cs96)? This issue is further investigated in  
 437 the following.

#### 438 4.2 Creation of temperature variance

The respective role of internal ocean dynamics and air-sea interactions in ex-  
 plaining the low-frequency oceanic variability is disentangled through the use of  
 the linearized temperature variance equation (Colin de Verdière and Huck, 1999;  
 Te Raa and Dijkstra, 2002; Arzel et al, 2006):

$$\overline{\partial_t \epsilon} = -\bar{\mathbf{u}} \cdot \nabla \bar{\epsilon} - \overline{\mathbf{u}'T'} \cdot \nabla \bar{T} + \overline{T'Q'} + \overline{T'D'} \quad (1)$$

439 where  $\epsilon = T'^2/2$  is the temperature variance, the overbar denotes a time average  
 440 over several oscillation periods and the prime the deviation from the time average  
 441 (i.e. yearly anomalies),  $\mathbf{u}$  and  $T$  the 3D velocity and temperature field,  $Q$  ocean-  
 442 atmosphere heat fluxes (positive downward) and  $D$  the oceanic diffusion. The  
 443 cubic eddy correlation terms are neglected because the perturbations observed  
 444 remain small compared to the mean state. The first term of the rhs represents the  
 445 transport of temperature variance by the mean flow  $\bar{\mathbf{u}}$ . It simply redistributes the  
 446 variance in the domain and cannot be a source of energy since it is zero globally.  
 447 The second term is a source of variability if the eddy temperature fluxes  $\overline{\mathbf{u}'T'}$  are  
 448 oriented down the mean temperature gradient  $\nabla\bar{T}$ . This term has been pinpointed  
 449 as the energy source for the variability under constant surface buoyancy fluxes in  
 450 the experiments of Colin de Verdière and Huck (1999) and Te Raa and Dijkstra  
 451 (2002). Under mixed surface boundary conditions by contrast, Arzel et al (2006)  
 452 identified a convective-surface heat flux feedback where the third term  $\overline{T'Q'}$  is the  
 453 driver of multidecadal variability (this term is discussed in section 4.2.2). The last  
 454 term  $\overline{(T'D')}$  represents a sink of energy due to diffusive and convective processes.  
 455 Therefore, determining which of the second or third terms (i.e. the only possible  
 456 sources of energy) in the rhs of (1) dominates the balance may help to elucidate  
 457 the physical mechanisms governing the variability.

#### 458 4.2.1 Internal oceanic dynamics

459 The role of oceanic dynamics is diagnosed following the work of Colin de Verdière  
 460 and Huck (1999). They show that in order for an instability to grow against mixing  
 461 and atmospheric damping, oceanic eddy temperature fluxes have to be oriented  
 462 down the mean temperature gradient, i.e.  $-\overline{\mathbf{u}'T' \cdot \nabla\bar{T}} > 0$  (see Eq. (1)). When

463 positive, this term represents a transfer of mean potential energy to eddy kinetic  
 464 and potential energy, which tends to relax mean temperature gradients. This term  
 465 indicates the regions of growth of the perturbations. Here, this term is computed  
 466 using the yearly temperature and velocities fields, and results are averaged over  
 467 the upper 1000 m (Fig. 11).

468 For cs24, the region where the magnitude of  $-\overline{\mathbf{u}'T' \cdot \nabla \overline{T}}$  is the largest is located  
 469 near the eastern boundary, around 60°N, in agreement with results of Buckley  
 470 et al (2012). For cs48 and cs96, this region shifts near the subpolar gyre western  
 471 boundary, between 50°-60°N. Averaged over the small basin,  $-\overline{\mathbf{u}'T' \cdot \nabla \overline{T}}$  is positive  
 472 in all set-ups, and is mainly driven by positive meridional eddy fluxes ( $\overline{v'T'}$ ),  
 473 oriented down the mean meridional temperature gradient ( $\partial_y \overline{T} < 0$ ). The zonal  
 474 and vertical contributions play a secondary role. Hence the growth of temperature  
 475 variance through large-scale baroclinic instability mostly takes place in the vicinity  
 476 of the western boundary for cs48 and cs96, but mostly along the eastern boundary  
 477 for cs24.

#### 478 4.2.2 Air-sea heat fluxes

479 At multidecadal timescales, the transfer of atmospheric variability into the ocean is  
 480 usually attributed to heat fluxes exchange (Timmermann et al, 1998; Delworth and  
 481 Greatbatch, 2000). These fluxes have also been pinpointed as a source of variability  
 482 for the oceanic low frequency variability under mixed surface boundary conditions  
 483 (Arzel et al, 2006). Such a transfer is diagnosed here by computing the correlation  
 484 between the surface heat flux anomalies ( $Q'$ ) and the SST anomalies ( $T'$ ), i.e. the  
 485 third term of the rhs of (1). Both heat fluxes and SST anomalies are filtered with  
 486 a 10 yr running mean, referred to as the long-term signal hereafter. Here,  $Q'$  is

487 positive downward for a heat flux from atmosphere to ocean:  $Q' \propto (T'_a - T')$ , with  
 488  $T'_a$  and  $T'$  the atmospheric and oceanic temperature at the interface, respectively.  
 489 Lets consider the case of a negative heat flux anomaly ( $Q' < 0$ ) with all other  
 490 fluxes at rest. It can either mean that the ocean is warmer than normal ( $T' > 0$   
 491 and  $T'_a = 0$ ) or that the atmosphere is colder than normal ( $T'_a < 0$  and  $T' = 0$ ).  
 492 In the case of  $T' > 0$ , the negative correlation  $T'Q' < 0$  results from oceanic  
 493 dynamics, and (1) shows that air-sea forcing is damping the low frequency oceanic  
 494 variability. On the other hand, if  $T'_a < 0$ , the atmosphere will extract heat from  
 495 the ocean, inducing  $T' < 0$  and hence a positive correlation  $T'Q' > 0$ . In the  
 496 framework of (1), the atmospheric variability will induce an oceanic variability  
 497 through heat fluxes. The same conclusions can be reached by considering the case  
 498 of positive heat fluxes anomalies. On long time cales, the small basin north of  $30^\circ\text{N}$   
 499 is dominated by negative correlations (Fig. 12, top row panels), indicating that the  
 500 ocean-atmosphere heat fluxes are driven by the oceanic dynamics. The third term  
 501 of (1) is then a sink for the oceanic low-frequency variability, and SST anomalies  
 502 observed in Fig. 8 are damped by atmospheric heat fluxes. Between  $10^\circ$ - $30^\circ\text{N}$ , we  
 503 observe a band of positive correlation ( $T'Q' > 0$ ). However, on these timescales,  
 504 tropical SST (Fig. 8) are not significantly correlated to the MOC variability. Such  
 505 a correlation between SST and heat fluxes short-term variability may then not  
 506 have a significant impact on the intrinsic oceanic low frequency MOC variability.

507 Using observational data, Gulev et al (2013) have confirmed the Bjerknes  
 508 (1964) assumption for the North Atlantic sector:  $Q'$  is driven by ocean dynamics on  
 509 long-term (multidecadal timescales), but by the atmospheric dynamics on short-  
 510 term (interannual to decadal timescales). To investigate this issue in our model,  
 511 we compute now the short-term signal by taking the deviation from the long-term

512 signal, i.e. the 10-yr-smoothed temperature and heat fluxes anomalies. The 10-yr  
513 smoothing window appears to be an ideal time filtering to clearly separate the  
514 oceanic and atmospheric role in the heat fluxes variability (Gulev et al, 2013).  
515 On short-term (Fig. 12, bottom row panels), the correlation is positive almost all  
516 over the small basin. At those timescales, ocean-atmosphere heat fluxes are mainly  
517 driven by the atmosphere, consistent with the stochastic forcing of the ocean in  
518 the Frankignoul and Hasselmann (1977)'s paradigm, and the results of Gulev et al  
519 (2013). However, a negative correlation is observed along the western boundary of  
520 the subpolar gyre, and spreads over a wider region as the resolution increases. In  
521 this region, the short-term heat fluxes variability is driven by the ocean dynamics  
522 rather than the atmosphere.

523 It has been proposed that OHT controls air-sea heat fluxes at interannual time  
524 scales in the Western North Atlantic, mainly through geostrophic advection (Dong  
525 et al, 2007; Buckley et al, 2015). This supports the idea that SST anomalies along  
526 the western boundary of the subpolar gyre observed in cs48 and cs96 (Fig. 8) result  
527 from OHT convergence at this location. The atmosphere damps the SST anoma-  
528 lies, resulting in a negative correlation  $T'Q' < 0$ . This correlation gets stronger with  
529 increasing resolution, but not the SST variability as described at the end of section  
530 3.2. Processes that are resolution dependent may also explain this increase in a  
531 negative correlation. Recent studies (Minobe et al, 2008; Skillingstad et al, 2007)  
532 show that sharp SST fronts typical of western boundary regions tend to destabi-  
533 lize the Marine Atmospheric Boundary Layer, resulting in atmospheric dynamics  
534 that are directly driven by the underlying ocean. In our model, the sharpening of  
535 SST gradients along the western boundary resulting from the increased oceanic  
536 resolution might induce a stronger atmospheric response, explaining the increased

537 correlation  $T'Q'$  at higher resolution. This atmospheric response could ultimately  
538 feedback into the ocean. However, such barely resolved processes are out of the  
539 scope of this paper.

#### 540 4.3 Ocean only experiments

541 To further investigate the influence of air-sea interactions for the low frequency  
542 oceanic variability in cs96, we have run an ocean-only experiment. The ocean is  
543 forced at the surface by 5-day climatological fresh water and momentum fluxes.  
544 The forcing in temperature is composed of a 5-days climatological flux term, and  
545 a restoring toward the 5-day climatological SST, with a time scale of about 72  
546 days (coupling coefficient  $\alpha = 20 \text{ W m}^{-2} \text{ K}^{-1}$  (Frankignoul et al, 1998)). All terms  
547 are extracted from the coupled model, which will be referred to as CPL hereafter.  
548 Oceanic initial conditions are the oceanic state of CPL after 400 yr of integration.  
549 This ocean-only experiment (referred to as CLIM-FLX hereafter) is integrated for  
550 200 yr. A similar experiment has been conducted by Buckley et al (2012) to show  
551 the intrinsic nature of the oceanic variability in cs24. Their ocean-only experi-  
552 ment reproduced in close agreement the low-frequency MOC variability of their  
553 flat bottom coupled configuration, demonstrating that the stochastic atmospheric  
554 forcing is not essential for the oceanic variability. Such a conclusion remains valid  
555 for cs96. The CLIM-FLX experiment reproduces relatively well the MOC variabil-  
556 ity of CPL, with a strong peak of variability at 43 yr (Fig. 13). As revealed by  
557 time series and power spectrum, the regularity of the MOC variations is strongly  
558 increased in CLIM-FLX, with less interannual variability, but almost the same  
559 energy at multidecadal time scales. Within the subpolar gyre, the propagation of

560 large scale baroclinic Rossby waves has a more regular signature (Fig. 7, bottom  
561 right panel), with an averaged phase velocity from eastern to western boundary  
562 of about  $0.33 \text{ cm s}^{-1}$ , just as in CPL. Consequently, air-sea interactions in CPL  
563 clearly disrupt the propagation of large scale baroclinic Rossby waves, perturbing  
564 the regularity of the MOC variability.

## 565 **5 Summary and discussion**

566 In this paper, we have investigated the role of air-sea interactions in the multi-  
567 decadal variability of the Meridional Overturning Circulation (MOC). We used  
568 both fully coupled and ocean only GCM runs with an idealized flat-bottom aqua-  
569 planet geometry and two meridional boundaries. This Double Drake configuration  
570 reproduces some aspects of the present climate (Ferreira et al, 2010). Three set-ups,  
571 with horizontal resolution of about  $4^\circ$ ,  $2^\circ$  and  $1^\circ$  (cs24, cs48 and cs96, respectively)  
572 in both the ocean and the atmosphere, are compared. Cs48 is run in a coupled  
573 configuration only, while both cs24 and cs96 are run in coupled and ocean-only  
574 configurations. By increasing the horizontal resolution in both the ocean and at-  
575 mosphere models, we have increased the intrinsic atmospheric variability, which  
576 is almost doubling from cs24 to cs96. In contrast, mesoscale eddies are still not  
577 resolved in the ocean. The main results can be summarized as follow:

- 578 1. In all coupled configurations, the MOC exhibits an intrinsic oceanic mode  
579 of variability on time scales of 30-40 yr. It is related to large-scale oceanic  
580 baroclinic Rossby waves that originate and propagate along the climatological  
581 mean zero-wind stress curl line, corresponding to the northern extent of the  
582 subpolar gyre.



- 583 2. Using a temperature variance budget, the origin of the multidecadal variabil-  
584 ity is identified as an internal oceanic mode sustained through the growth of  
585 large-scale baroclinic Rossby waves, while air-sea interactions have a damp-  
586 ing influence. The growth of baroclinic Rossby waves mostly takes place in  
587 the vicinity of the western boundary for cs48 and cs96, but mostly along the  
588 eastern boundary for cs24.
- 589 3. In concert with increased intrinsic atmospheric variability, we found in cs96 a  
590 statistically significant correlation between the Northern Annular-Mode (NAM)  
591 and the MOC variability when the NAM leads by 2 yr.
- 592 4. The effect of atmospheric coupling tends to perturb the propagation of oceanic  
593 large-scale baroclinic Rossby waves across the basin in cs96, destabilizing the  
594 regularity of the oceanic oscillations. In this set-up, the MOC variability is an  
595 intrinsic oceanic mode, despite significant lag correlations between the NAM  
596 and the MOC.

597 The robustness of the multidecadal MOC variability reproduced in all flat  
598 bottom coupled configurations presented in this study complements the ocean-  
599 only experiments forced by fixed surface fluxes (Colin de Verdière and Huck, 1999),  
600 coupled to an atmospheric energy balance model (Huck et al, 2001; Fanning and  
601 Weaver, 1998), or coupled to a zonally averaged atmospheric model (Arzel et al,  
602 2007). By coupling the ocean to a dynamical atmospheric component, we have  
603 climbed a further step in the realism of ocean-atmosphere interactions, and yet  
604 the same mechanism appears to be at work.

605 The development in cs96 of atmospheric variability that is significantly cor-  
606 related to the MOC variability highlights the importance of a sufficiently high

607 horizontal resolution to reproduce ocean-atmosphere interactions at decadal time  
608 scales. A similar conclusion has been reached by Hodson and Sutton (2012) using  
609 the realistic HadGEM2.1 coupled model run at two different horizontal resolutions  
610 ( $1^\circ$  and  $\frac{1}{3}^\circ$ ): The atmospheric pattern correlated to the low-frequency oceanic vari-  
611 ability is much more significant at higher resolution. Such a correlation is a robust  
612 feature of many high resolution realistic models (Eden and Willebrand, 2001; De-  
613 shayes and Frankignoul, 2008; Gastineau and Frankignoul, 2012), with a positive  
614 phase of the NAO that occurs few years prior a MOC maximum. These studies  
615 describe the MOC variability in the Atlantic as an oceanic response to the at-  
616 mospheric forcing, through a fast oceanic barotropic response to NAO-induced  
617 surface wind stress. A similar connection is drawn by Sun et al (2015) in their  
618 delayed oscillator model to explain the NAO low-frequency variability, but in-  
619 volves a time delay between the NAO and the Atlantic MOC of about 15 yr. Here,  
620 conducting an ocean-only simulation forced by constant fluxes for cs96 (denoted  
621 as CLIM-FLX), we prove that a significant lag correlation between SLPA and  
622 MOC does not imply that the oceanic low frequency variability is forced by the  
623 atmosphere. These results contrast with those of Delworth and Greatbatch (2000)  
624 who found in the GFDL coupled model that the 40-80 yr MOC variability mainly  
625 results from ocean-atmosphere heat fluxes driven by the intrinsic atmospheric  
626 low-frequency variability. Here, we have shown that at multidecadal time scales,  
627 ocean-atmosphere heat fluxes in the northern Atlantic basin are a consequence  
628 rather than a cause of internally driven ocean variability. Air-sea interactions are  
629 not crucial for the existence of the low frequency mode, but impact its expression.

630 These results may be discussed in two ways. First, even if the correlation be-  
631 tween the atmospheric and oceanic low frequency variability is strongly enhanced

632 at increasing resolution, the atmospheric response in the Double Drake model  
633 might remain too weak to efficiently influence the ocean mode. By increasing the  
634 horizontal resolution up to  $1^\circ$ , we have doubled the intrinsic atmospheric variabil-  
635 ity, but this resolution remains beyond the one necessary to significantly capture,  
636 for instance, the impact of oceanic fronts onto the atmosphere, maybe around 50  
637 km (Minobe et al, 2008). Those small scale ocean-atmosphere interactions might  
638 be of primary importance to reproduce an active atmosphere dynamics setting  
639 the oceanic low-frequency variability. However, studies that describe the multi-  
640 decadal climate variability as a coupled mode or as an oceanic mode forced by  
641 atmospheric variability do not claim the necessity of such small scale processes.  
642 They usually involve large scale ocean-atmosphere interactions. For instance, Tim-  
643 mermann et al (1998) described a coupled mode of variability in the  $4^\circ$  horizontal  
644 resolution ECHAM-3/LSG coupled model, such that large scale ocean atmosphere  
645 interactions between extratropical SST and atmospheric dynamics can be sufficient  
646 to generate a coupled mode of variability.

647 Secondly, the mechanisms proposed in high resolution climate model studies  
648 are rarely related to the propagation of Rossby waves. Indeed, Winton (1997) show  
649 that the ocean bathymetry may damp the intrinsic oceanic variability. In the same  
650 Double Drake model (the one used in this study), Buckley et al (2012) have shown  
651 that the introduction of an idealized bowl bathymetry switches the type of mode  
652 of variability from an ocean-only mode damped by atmospheric fluxes (with flat-  
653 bottom), to a damped oceanic mode stochastically excited by atmospheric fluxes  
654 (with bowl bathymetry). The impact of the bottom topography on the MOC vari-  
655 ability is principally attributed to the disruptive effect of the topography on the  
656 propagation of large-scale baroclinic Rossby waves. These results cast some doubt

657 on the **existence of these waves** in realistic climate models or in the real ocean.  
658 However, using observational data, Frankcombe et al (2008) observed the signature  
659 of large-scale SST and Sea Surface Height anomalies, propagating westward across  
660 the North Atlantic ocean. In addition, Sévellec and Fedorov (2013) show that, in a  
661  $2^\circ$  global configuration of the OPA (Océan PARallélisé) model with realistic topog-  
662 raphy, the least damped mode of variability of the tangent adjoint linear model  
663 remains a potential candidate to explain the MOC multidecadal variability (Or-  
664 tega et al, 2015). This mode is characterized by large-scale temperature anomalies  
665 that propagate westward across the subpolar gyre, associated with long baroclinic  
666 Rossby waves (Sévellec and Huck, 2015). It will be important to see how a realistic  
667 oceanic topography might influence the oceanic mechanism found in this study.

668 **Acknowledgements** We acknowledge the help from John Marshall, David Ferreira and  
669 Martha Buckley at MIT for providing the Double Drake model used in this study as well  
670 as post-processing routines, and for assistance in understanding the MITgcm environment.  
671 We thank the MIT EAPS group for hosting Q. Jamet when setting up cs48 and cs96 con-  
672 figurations. We also thank Guillaume Gastineau at LOCEAN/IPSL for providing routines to  
673 compute the statistical significance test, as well as for constructive discussions. Computational  
674 resources were provided by the Pôle de Calcul Intensif pour la Mer at Ifremer, Brest, France,  
675 and through a GENCI allocation attributed to O. Arzel.

---

676 **Appendix 1: Statistical significance test using Monte Carlo approach**

677 The significance of a regression or a correlation is computed with a Monte Carlo approach. It  
 678 consists in comparing the regression/correlation being tested to the regression/correlation of  
 679 a randomly scrambled ensemble. Say we want to estimate the significance of the regression of  
 680 a field  $\lambda(x, y, t)$  onto a time series (usually the Meridional Overturning Circulation)  $MOC(t)$ ,  
 681  $t$  being the time in yr,  $x$  and  $y$  the zonal and meridional coordinates. We first compute the  
 682 initial regression maps, denoted as  $reg_{init}(x, y)$ .

683 At each grid point  $(x_i, y_j)$ , the time series  $\lambda(x_i, y_j, t)$  is randomly permuted by blocks of  
 684 3 yr to reduce the influence of serial autocorrelation. The regression  $reg_{k1}(x_i, y_j)$  between the  
 685 resulting time series  $\lambda_{permut}(x_i, y_j, t)$  and  $MOC(t)$  is performed. This analysis is repeated  $N$   
 686 times, resulting in  $N$  different randomly permuted regression  $reg_k(x_i, y_j)$ ,  $k = (k_1, k_2, \dots, k_N)$ .  
 687 The estimated significance level is the percentage of randomized regression that exceeds the  
 688 regression being tested:

$$signif(x_i, y_j) = \frac{\sum_{k=1}^N reg_k(x_i, y_j) > reg_{init}(x_i, y_j)}{N} \quad (2)$$

689 A smaller significance level indicates the presence of stronger evidence against the null  
 690 hypothesis. In this paper, we fix the threshold of significance to 5%. This statistical significant  
 691 test is applied for all regression / correlation analyses performed.

692 **Appendix 2: MOC anomalies reconstruction from the difference between**  
 693 **density/temperature anomalies along the western and eastern boundaries**

694 Hirschi and Marotzke (2007) show that the MOC variability can be reconstructed through  
 695 the thermal wind relationship by considering boundary density anomalies. This reconstruction  
 696 does include neither the Ekman shear mode nor the barotropic velocities. In flat bottom  
 697 configuration, the latter is strictly zero, which facilitates the reconstruction in our case.

The thermal wind relationship

$$f\partial_z v = -\frac{g}{\rho_0}\partial_x \rho, \quad (3)$$

is used as the starting point, with  $f$  the Coriolis parameter,  $v$  the meridional velocity,  $g$  the earth's acceleration,  $\rho$  the density and  $\rho_0$  its reference value. Integrating zonally and vertically the perturbation part of Eq. (3), with the condition  $v'(z = -H) = 0$ , leads to

$$\overline{v'(z')^x} = \int_{x_w}^{x_e} v' dx = -\frac{g}{\rho_0 f} \int_{-H}^{z'} (\rho'_e - \rho'_w) dz \quad (4)$$

We reconstruct a geostrophic MOC anomaly  $\psi_\rho^*$  as the vertical integration of  $\overline{v'(z')^x}$ :

$$\psi_\rho^*(z') = \int_{-H}^{z'} \left[ \overline{v'^x} - \frac{1}{H} \int_{-H}^0 \overline{v'^x} dz \right] dz, \quad (5)$$

698 where  $\frac{1}{H} \int_{-H}^0 \overline{v'^x} dz$  has been subtracted in order to ensure that  $\psi_\rho^*(z' = 0) = \psi_\rho^*(z' = -H) =$   
 699 0.

We can go a step further in the approximation by only considering the temperature contribution. The thermal wind relationship reduces to

$$f\partial_z v = g\alpha\partial_x T \quad (6)$$

with  $\alpha = 2.10^{-4} K^{-1}$ , the thermal expansion coefficient. Performing a similar integration, we obtain a reconstructed MOC anomaly  $\psi_T^*$  computed with a zonally integrated meridional velocities anomalies of the form

$$\overline{v'(z')^x} = \int_{x_w}^{x_e} v' dx = \frac{g\alpha}{f} \int_{-H}^{z'} (T'_e - T'_w) dz, \quad (7)$$

700 with  $T'_e$  and  $T'_w$  the temperature anomalies along the eastern and western boundaries, re-  
 701 spectively. We can also compute the contribution from the western boundary temperature  
 702 anomalies only,  $\psi_{T_w}^*$ .

703 Note that this method misses one half grid point at the eastern and western boundaries.  
 704 Both temperature and density anomalies that are used to reconstruct the MOC variability are  
 705 located at the centre of the cell, rather than right along boundaries. This error is dependent  
 706 on the horizontal resolution, and partially explains why the reconstructions are more accurate  
 707 at higher resolution.

The geostrophic MOC indices are computed in the same way as for the model. The skill for the geostrophic MOC index ( $I_{\psi^*}$ ) accounting for the variance of the model MOC index ( $I_{MOC}$ ) is defined as

$$S = 1 - \frac{\langle (I_{MOC} - I_{\psi^*})^2 \rangle}{\langle I_{MOC}^2 \rangle} \quad (8)$$

708 with  $\langle . \rangle$  a time average operator.  $S \in [-\infty; 1]$ , and  $S \rightarrow 1$  indicates that the geostrophic  
 709 MOC index and the model MOC index vary in phase and are of the same magnitude. Negative  
 710 values denote a low or negative correlation and/or that the amplitude of  $I_{\psi^*}$  is larger than  
 711  $I_{MOC}$ .

712 **References**

- 713 Adcroft A, Campin JM, Hill C, Marshall J (2004) Implementation of an atmosphere-ocean  
714 general circulation model on the expanded spherical cube. *Mon Wea Rev* 132(12):2845–  
715 2863
- 716 Arakelian A, Codron F (2012) Southern Hemisphere Jet Variability in the IPSL GCM at  
717 Varying Resolutions. *J Atmos Sci* 69:3788–3799
- 718 Arzel O, Huck T, Colin de Verdière A (2006) The Different Nature of the Interdecadal Variabil-  
719 ity of the Thermohaline Circulation under Mixed and Flux Boundary Conditions. *J Phys*  
720 *Oceanogr* 36:1703–1718
- 721 Arzel O, Colin de Verdière A, Huck T (2007) On the origin of interdecadal oscillations in a  
722 coupled ocean–atmosphere model. *Tellus* 59A:367–383
- 723 Arzel O, England MH, Colin de Verdière A, Huck T (2012) Abrupt millennial variability and  
724 interdecadal-interstadial oscillations in a global coupled model: sensitivity to the background  
725 climate state. *Clim Dyn* 39:259–275
- 726 Bjerknes J (1964) Atlantic air-sea interaction. *Advances in geophysics* 10(1):1–82
- 727 Buckley MW, Ferreira D, Campin JM, Marshall J, Tulloch R (2012) On the relationship  
728 between decadal buoyancy anomalies and variability of the Atlantic meridional overturning  
729 circulation. *J Clim* 25(23):8009–8030
- 730 Buckley MW, Ponte RM, Forget G, Heimbach P (2015) Determining the origins of advective  
731 heat transport convergence variability in the North Atlantic. *J Clim* (2015)
- 732 Chylek P, Folland CK, Dijkstra HA, Lesins G, Dubey MK (2011) Ice-core data evidence for  
733 a prominent near 20 year time-scale of the Atlantic Multidecadal Oscillation. *Geophys Res*  
734 *Lett* 38(L13704)
- 735 Colin de Verdière A, Huck T (1999) Baroclinic instability: An oceanic wavemaker for inter-  
736 decadal variability. *J Phys Oceanogr* 29(5):893–910
- 737 Danabasoglu G (2008) On multidecadal variability of the Atlantic meridional overturning  
738 circulation in the community climate system model version 3. *J Clim* 21(21):5524–5544
- 739 Delworth T, Manabe S, Stouffer R (1993) Interdecadal variations of the thermohaline circula-  
740 tion in a coupled ocean-atmosphere model. *J Clim* 6(11):1993–2011



- 741 Delworth TL, Greatbatch RJ (2000) Multidecadal thermohaline circulation variability driven  
742 by atmospheric surface flux forcing. *J Clim* 13(9):1481–1495
- 743 Delworth TL, Zhang R, Mann ME (2007) Decadal to centennial variability of the Atlantic from  
744 observations and models. *Geophysical Monograph* 173:131–148, ocean circulation: Mecha-  
745 nisms and Impacts
- 746 Deser C (2000) On the teleconnectivity of the Arctic Oscillation. *Geophys Res Lett* 27(6):779–  
747 782
- 748 Deshayes J, Frankignoul C (2008) Simulated variability of the circulation in the North Atlantic  
749 from 1953 to 2003. *J Clim* 21(19):4919–4933
- 750 Dong S, Hautala SL, Kelly KA (2007) Interannual variations in upper-ocean heat content and  
751 heat transport convergence in the western North Atlantic. *J Phys Oceanogr* 37(11):2682–  
752 2697
- 753 Eden C, Jung T (2001) North Atlantic interdecadal variability: Oceanic response to the North  
754 Atlantic Oscillation (1865-1997). *J Clim* 14:676–691
- 755 Eden C, Willebrand J (2001) Mechanism of interannual to decadal variability of the north  
756 atlantic circulation. *J Clim* 14(10):2266–2280
- 757 Enfield DB, Mestas-Nuñez AM, Trimble PJ (2001) The Atlantic multidecadal oscillation and  
758 its relation to rainfall and river flows in the continental US. *Geophys Res Lett* 28(10):2077–  
759 2080
- 760 Fanning AF, Weaver AJ (1998) Thermohaline variability: The effects of horizontal resolution  
761 and diffusion. *J Clim* 11(4):709–715
- 762 Ferreira D, Marshall J, Campin JM (2010) Localization of deep water formation: Role of  
763 atmospheric moisture transport and geometrical constraints on ocean circulation. *J Clim*  
764 23(6):1456–1476
- 765 Folland C, Palmer T, Parker D (1986) Sahel rainfall and worldwide sea temperatures, 1901–85.  
766 *Nature* 320(6063):602–607
- 767 Frankcombe L, Dijkstra H (2009) Coherent multidecadal variability in North Atlantic sea level.  
768 *Geophys Res Lett* 36(L15604)
- 769 Frankcombe L, Dijkstra H, Von der Heydt A (2008) Sub-surface signatures of the Atlantic  
770 Multidecadal Oscillation. *Geophys Res Lett* 35(L19602)

- 771 Frankcombe LM, Dijkstra HA, Von der Heydt A (2009) Noise-induced multidecadal variability  
772 in the North Atlantic: Excitation of normal modes. *J Phys Oceanogr* 39(1):220–233
- 773 Frankcombe LM, Von Der Heydt A, Dijkstra HA (2010) North Atlantic multidecadal climate  
774 variability: an investigation of dominant time scales and processes. *J Clim* 23(13):3626–3638
- 775 Frankignoul C, Hasselmann K (1977) Stochastic climate models, part ii application to sea-  
776 surface temperature anomalies and thermocline variability. *Tellus* 29(4):289–305
- 777 Frankignoul C, Czaja A, L’Heveder B (1998) Air-sea feedback in the North Atlantic and surface  
778 boundary conditions for ocean models. *J Clim* 11(9):2310–2324
- 779 Gastineau G, Frankignoul C (2012) Cold-season atmospheric response to the natural variability  
780 of the Atlantic meridional overturning circulation. *Clim Dyn* 39(1-2):37–57
- 781 Gent PR, McWilliams JC (1990) Isopycnal mixing in ocean circulation models. *J Phys*  
782 *Oceanogr* 20(1):150–155
- 783 Griffies SM, Tziperman E (1995) A linear thermohaline oscillator driven by stochastic atmo-  
784 spheric forcing. *J Clim* 8:2440–2453
- 785 Gulev SK, Latif M, Keenlyside N, Park W, Koltermann KP (2013) North Atlantic Ocean  
786 control on surface heat flux on multidecadal timescales. *Nature* 499(7459):464–467
- 787 Harnik N, Chang EK (2004) The effects of variations in jet width on the growth of baroclinic  
788 waves: Implications for midwinter Pacific storm track variability. *J Atmos Sci* 61(1):23–40
- 789 Hirschi J, Marotzke J (2007) Reconstructing the meridional overturning circulation from  
790 boundary densities and the zonal wind stress. *J Phys Oceanogr* 37(3):743–763
- 791 Hodson DL, Sutton RT (2012) The impact of resolution on the adjustment and decadal vari-  
792 ability of the Atlantic meridional overturning circulation in a coupled climate model. *Clim*  
793 *Dyn* 39(12):3057–3073
- 794 Huck T, Vallis GK, Colin de Verdière A (2001) On the robustness of the interdecadal modes  
795 of the thermohaline circulation. *J Clim* 14(5):940–963
- 796 Huck T, Arzel O, Sévellec F (2015) Multidecadal variability of the overturning circulation in  
797 presence of eddy turbulence. *J Phys Oceanogr* 45(1):157–173
- 798 Hurrell JW (1995) Decadal trends in the North Atlantic Oscillation: regional temperatures  
799 and precipitation. *Science* 269(5224):676–679

- 800 Kerr RA (2000) A North Atlantic climate pacemaker for the centuries. *Science* 288(5473):1984–  
801 1985
- 802 Knight JR, Allan RJ, Folland CK, Vellinga M, Mann ME (2005) A signature of persistent  
803 natural thermohaline circulation cycles in observed climate. *Geophys Res Lett* 32(L20708)
- 804 Kushnir Y (1994) Interdecadal variations in North Atlantic sea surface temperature and asso-  
805 ciated atmospheric conditions. *J Clim* 7(1):141–157
- 806 Kushnir Y, Robinson WA, Blad I, Hall NMJ, Peng S, Sutton R (2002) Atmospheric gcm  
807 response to extratropical sst anomalies: synthesis and evaluation. *J Clim* 15:2233–2256
- 808 Liu Z (2012) Dynamics of Interdecadal Climate Variability: A Historical Perspective\*. *J Clim*  
809 25(6):1963–1995
- 810 Marsh R, de Cuevas BA, Coward AC, Jacquin J, Hirschi JJM, Aksenov Y, Nurser A, Josey  
811 SA (2009) Recent changes in the North Atlantic circulation simulated with eddy-permitting  
812 and eddy-resolving ocean models. *Ocean Model* 28(4):226–239
- 813 Marshall J, Adcroft A, Hill C, Perelman L, Heisey C (1997) A finite-volume, incompress-  
814 ible Navier Stokes model for studies of the ocean on parallel computers. *J Geophys Res*  
815 102(C3):5753–5766
- 816 McCarthy GD, Haigh ID, Hirschi JJM, Grist JP, Smeed DA (2015) Ocean impact on decadal  
817 Atlantic climate variability revealed by sea-level observations. *Nature* 521(7553):508–510
- 818 Mecking J, Keenlyside NS, Greatbatch RJ (2014) Stochastically-forced multidecadal variability  
819 in the north atlantic: a model study. *Clim Dyn* 43:271–288
- 820 Minobe S, Kuwano-Yoshida A, Komori N, Xie SP, Small RJ (2008) Influence of the gulf stream  
821 on the troposphere. *Nature* 452(7184):206–209
- 822 Molteni F (2003) Atmospheric simulations using a GCM with simplified physical parametriza-  
823 tions. I: Model climatology and variability in multi-decadal experiments. *Clim Dyn* 20(2-  
824 3):175–191
- 825 Ollitrault M, Colin de Verdière A (2002) SOFAR floats reveal midlatitude intermediate  
826 North Atlantic general circulation. Part II: An Eulerian statistical view. *J Phys Oceanogr*  
827 32(7):2034–2053
- 828 Ortega P, Mignot J, Swingedouw D, Sévellec F, Guilyardi E (2015) Reconciling two alternative  
829 mechanisms behind bi-decadal AMOC variability. *Prog Oceanogr* (in revision)

- 830 Penduff T, Juza M, Barnier B, Zika J, Dewar WK, Treguier AM, Molines JM, Audiffren N  
831 (2011) Sea level expression of intrinsic and forced ocean variabilities at interannual time  
832 scales. *J Clim* 24(21):5652–5670
- 833 Pope V, Stratton R (2002) The processes governing horizontal resolution sensitivity in a climate  
834 model. *Clim Dyn* 19(3-4):211–236
- 835 Redi MH (1982) Oceanic isopycnal mixing by coordinate rotation. *J Phys Oceanogr*  
836 12(10):1154–1158
- 837 Schlesinger ME, Ramankutty N (1994) An oscillation in the global climate system of period  
838 65–70 years. *Nature* 367(6465):723–726
- 839 Sévellec F, Fedorov AV (2013) The leading, interdecadal eigenmode of the Atlantic meridional  
840 overturning circulation in a realistic ocean model. *J Clim* 26(7):2160–2183
- 841 Sévellec F, Huck T (2015) Theoretical Investigation of the Atlantic Multidecadal Oscillation.  
842 *J Phys Oceanogr* (2015)
- 843 Sévellec F, Huck T, Ben Jelloul M, Vialard J (2009) Nonnormal multidecadal response of the  
844 thermohaline circulation induced by optimal surface salinity perturbations. *J Phys Oceanogr*  
845 39(4):852–872
- 846 Skyllingstad ED, Vickers D, Mahrt L, Samelson R (2007) Effects of mesoscale sea-surface  
847 temperature fronts on the marine atmospheric boundary layer. *Bound Layer Meteorol*  
848 123(2):219–237
- 849 Sun C, Li J, Jin FF (2015) A delayed oscillator model for the quasi-periodic multidecadal  
850 variability of the NAO. *Clim Dyn* pp 1–17
- 851 Sutton RT, Hodson DL (2005) Atlantic Ocean forcing of North American and European sum-  
852 mer climate. *Science* 309(5731):115–118
- 853 Te Raa LA, Dijkstra HA (2002) Instability of the thermohaline ocean circulation on inter-  
854 decadal timescales. *J Phys Oceanogr* 32(1):138–160
- 855 Thompson DW, Wallace JM (1998) The arctic oscillation signature in the wintertime geopo-  
856 tential height and temperature fields. *Geophys Res Lett* 25(9):1297–1300
- 857 Thompson DW, Wallace JM (2001) Regional climate impacts of the Northern Hemisphere  
858 annular mode. *Science* 293(5527):85–89

- 
- 859 Timmermann A, Latif M, Voss R, Grötzner A (1998) Northern hemispheric interdecadal vari-  
860 ability: a coupled air-sea mode. *J Clim* 11(8):1906–1931
- 861 Trenberth K, Caron J, Stepaniak D (2001) The atmospheric energy budget and implications  
862 for surface fluxes and ocean heat transports. *Clim Dyn* 17(4):259–276
- 863 Tulloch R, Marshall J (2012) Exploring mechanisms of variability and predictability of Atlantic  
864 meridional overturning circulation in two coupled climate models. *J Clim* 25(12):4067–4080
- 865 Vallis GK, Gerber EP, Kushner PJ, Cash BA (2004) A mechanism and simple dynamical  
866 model of the North Atlantic Oscillation and annular modes. *J Atmos Sci* 61(3):264–280
- 867 Weaver AJ, Valcke S (1998) On the variability of the thermohaline circulation in the GFDL  
868 coupled model. *J Clim* 11(4):759–767
- 869 Winton M (1997) The damping effect of bottom topography on internal decadal-scale oscilla-  
870 tions of the thermohaline circulation. *J Phys Oceanogr* 27(1):203–208
- 871 Zhang R (2008) Coherent surface-subsurface fingerprint of the Atlantic meridional overturning  
872 circulation. *Geophys Res Lett* 35(L20705)
- 873 Zhang R (2010) Latitudinal dependence of Atlantic meridional overturning circulation  
874 (AMOC) variations. *Geophys Res Lett* 37(L16703)

**Table 1** Main characteristics of oceanic and atmospheric components of the Double Drake configuration at three different resolutions. From left to right: name of the set-up, horizontal resolution (in  $^{\circ}$ ), oceanic and atmospheric time step (s), transfer coefficient for eddy-induced advection and diffusion processes ( $\text{m}^2 \text{s}^{-1}$ ), horizontal viscosity ( $\text{m}^2 \text{s}^{-1}$ ), time integration (yr), and standard deviation  $\sigma$  of yearly MOC and NAM indices. The latter is computed with the absolute maximum of the spatial EOF1 pattern obtained with a projection onto the standardized PC1. The first EOF/PC is computed on the yearly SLPA over the north hemisphere only

model	$\Delta x$	$\Delta t$		Ocn GM	$\nu_{ocn}$	Integration	$\sigma_{MOC}$	$\sigma_{NAM}$
set-up	(deg)	Ocn (s)	Atm (s)	( $\text{m}^2 \text{s}^{-1}$ )	( $\text{m}^2 \text{s}^{-1}$ )	(yr)	(Sv)	(hPa)
cs24	$\sim 3.8^{\circ}$	3600	1200	1200	$3.10^5$	600	0.95	2.98
cs48	$\sim 1.9^{\circ}$	2400	400	1200	$1.10^5$	600	1.76	4.13
cs96	$\sim 0.9^{\circ}$	2400	200	1200	$4.10^4$	600	1.91	5.39

**Table 2** Correlation between the yearly MOC index of Buckley et al (2012), defined as the average of the small basin MOC in the box [8°-60°N, 460-1890 m depth] (black box in Fig. 2, bottom panels), and 8 other yearly time series related to the overturning: 1/ a western boundary velocity index (WBC, defined as meridional velocities anomaly along the western boundary at 30°N, averaged in the upper 1000 m), 2/ the maximum of the MOC within the box [8°-60°N, 460-1890 m depth] (allowing spatial variations of its location (Marsh et al, 2009)), 3/ the Principal Component (PC) of the first Empirical Orthogonal Function (EOF) of the MOC streamfunction within the small basin, north of 34°S (explaining more than 60% of the variance) and 4/ the maximum of the mean MOC at 5 given latitudes (21°N, 30°N, 42°N, 50°N and 63°N). At 63°N, the MOC is in advance of a couple of years compared to the initial MOC index, as illustrated on Fig. 8 of Buckley et al (2012) for cs24. This lag between MOC anomalies at various latitudes explains the lower correlation found at high latitudes. In addition, all latitudes from 8-60°N are integrated into the original MOC index, while the MOC variability at 63°N is not considered

	<i>WBC</i>	<i>MOC<sub>max</sub></i>	<i>PC<sub>1</sub><sup>moc</sup></i>	<i>MOC<sub>21N</sub></i>	<i>MOC<sub>30N</sub></i>	<i>MOC<sub>42N</sub></i>	<i>MOC<sub>50N</sub></i>	<i>MOC<sub>63N</sub></i>
cs24	$r = 0.80$	0.91	0.99	0.91	0.90	0.91	0.80	0.37
cs48	$r = 0.80$	0.98	0.99	0.98	0.97	0.97	0.95	0.76
cs96	$r = 0.80$	0.97	0.97	0.97	0.97	0.96	0.96	0.77

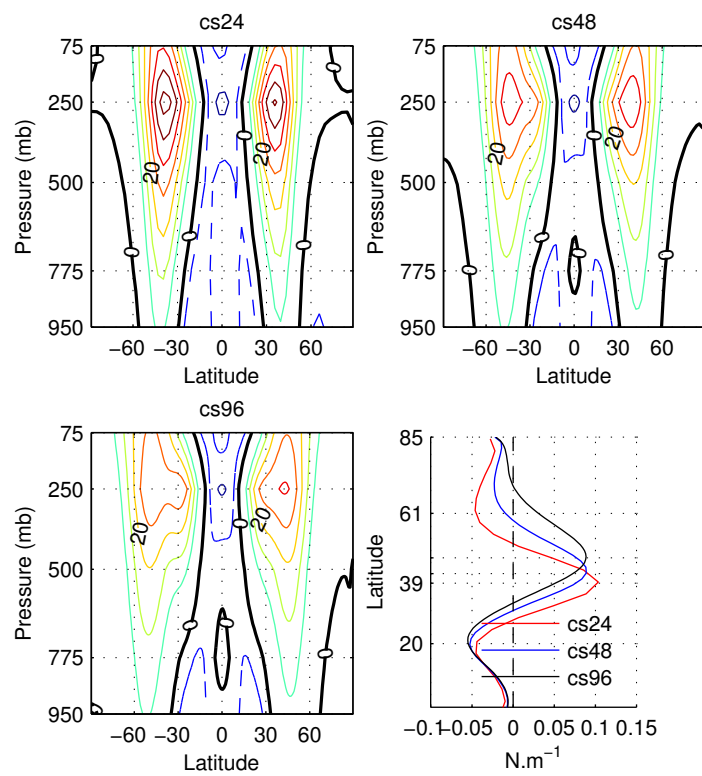


**Fig. 1** Zonal mean zonal winds for cs24 (top left), cs48 (top right) and cs96 (bottom left). The contour interval is  $5 \text{ m s}^{-1}$ , negative values are dashed lines, and the zero contour is thick black line. (bottom right) Zonal surface wind stress zonally averaged over the small basin. Maximum of the eastward surface wind stress is at  $39^\circ\text{N}$ ,  $42^\circ\text{N}$  and  $47^\circ\text{N}$  for cs24, cs48 and cs96, respectively. Extrema for cs24 are labelled on the y axis



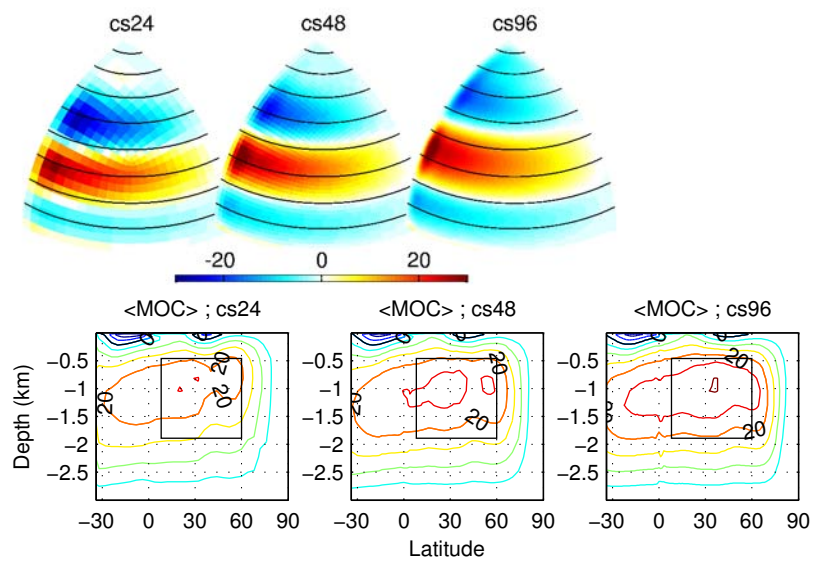


**Fig. 2** (top panels) Barotropic streamfunction in Sv ( $1 \text{ Sv} = 10^6 \text{ m}^3 \text{ s}^{-1}$ ) within the small basin flat-bottom ocean; thin black contours mark latitude circles every  $10^\circ$  from  $10^\circ\text{N}$  to  $80^\circ\text{N}$ . (bottom panels) Meridional Overturning Circulation (MOC) in Sv within the small basin; the black box represents the region [ $8^\circ$ - $60^\circ\text{N}$ ; 460-1890 m depth] used to define the MOC index. The contour interval is 5 Sv and the zero contour is black. All fields are time mean over the last 400 yr of integrations

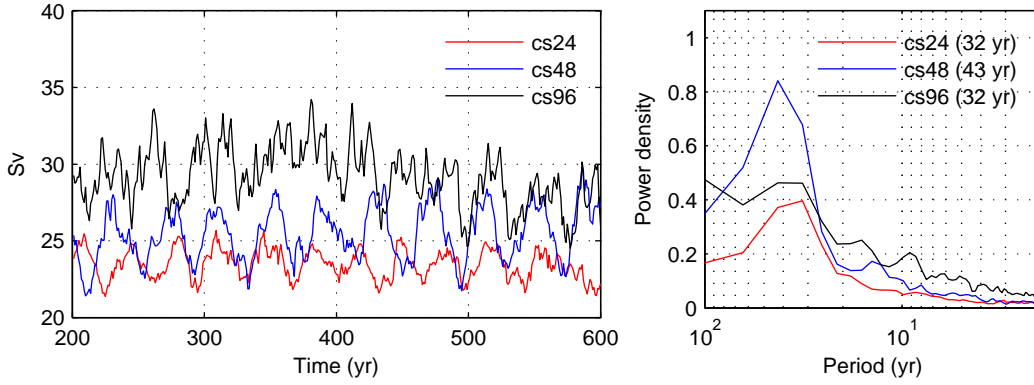


**Fig. 3** Yearly MOC time series in the box  $[8^{\circ}\text{-}60^{\circ}\text{N}; 460\text{-}1890\text{m}]$  (black box on Fig 2, bottom panels; see text for details) in Sv for all three set-ups (left) and their respective power spectrum (right). The time scale of the dominant period for each time series is displayed on the right panel.

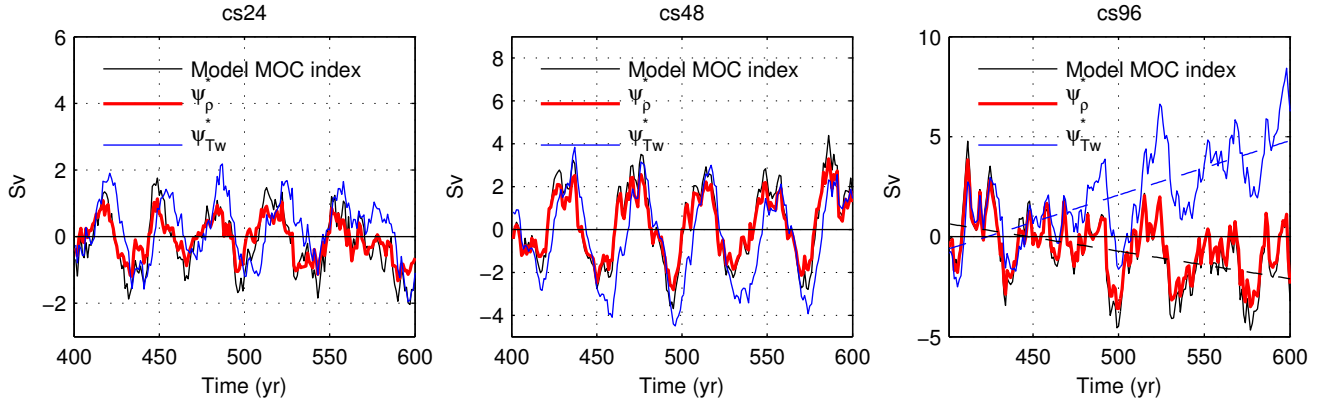


**Fig. 4** Reconstruction of the MOC index (model, black line) using the thermal wind relationship with density anomalies along eastern and western boundaries ( $\psi_{\rho}^*$ , red) and temperature anomalies along the western boundary ( $\psi_{T_w}^*$ , blue) for cs24 (left), cs48 (centre) and cs96 (right). See Appendix 2 for details. For cs24 (respectively cs48, cs96), the correlation is  $r = 0.92$  (0.99, 0.99) and 0.66 (0.82, 0.78) for the MOC index reconstructed from  $\psi_{\rho}^*$  and  $\psi_{T_w}^*$ , respectively. To compute the skill/correlation related to  $\psi_{T_w}^*$ , both the model and reconstructed MOC indices have been linearly detrended for cs96 (black and blue dashed lines on the right panel).

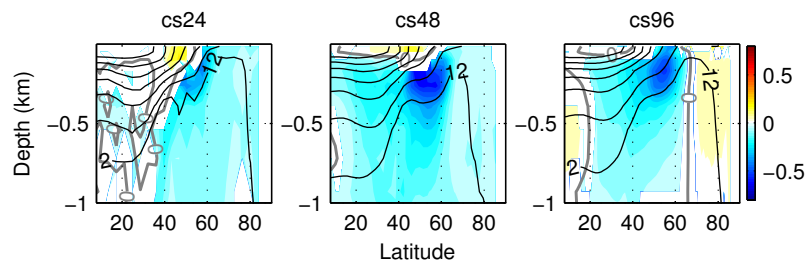


**Fig. 5** Yearly temperature anomalies along the western boundary (K) in the upper 1500 m associated with one standard deviation of the yearly MOC index at lag=0, for cs24 (left), cs48 (centre) and cs96 (right). Regions that are not statistically significant at 5% level are white shaded, and the zero regression is thick grey line. Black contours represent the mean potential temperature along the boundary. Contour interval is 3 K

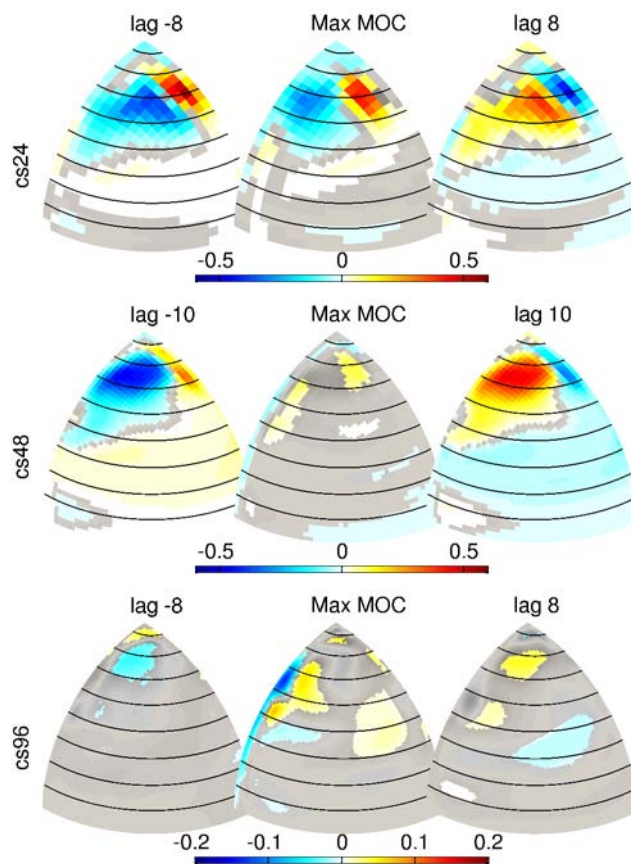


**Fig. 6** Yearly oceanic potential temperature anomalies averaged over the upper 1000 m ( $T_{1000}$ , in K) associated with one standard deviation of the yearly MOC index for cs24 (top row panels), cs48 (middle row) and cs96 (bottom row). Center panels correspond to  $lag = 0$ , while left (right) panels correspond to  $lag = -\frac{1}{4}T$  ( $lag = +\frac{1}{4}T$ ), with  $T$  the dominant period of the MOC variability estimated from the MOC index power spectrum (i.e., 32 yr for both cs24 and cs96, 43 yr for cs48).  $lag = -\frac{1}{4}T$  ( $lag = +\frac{1}{4}T$ ) corresponds to a strengthening (weakening) MOC. Regions that are not statistically significant at the 5% level are grey shaded (see Appendix 1 for details). Thin black contours mark latitude circles every  $10^\circ$  from  $10^\circ\text{N}$  to  $80^\circ\text{N}$ . Note the different colour axis for cs96

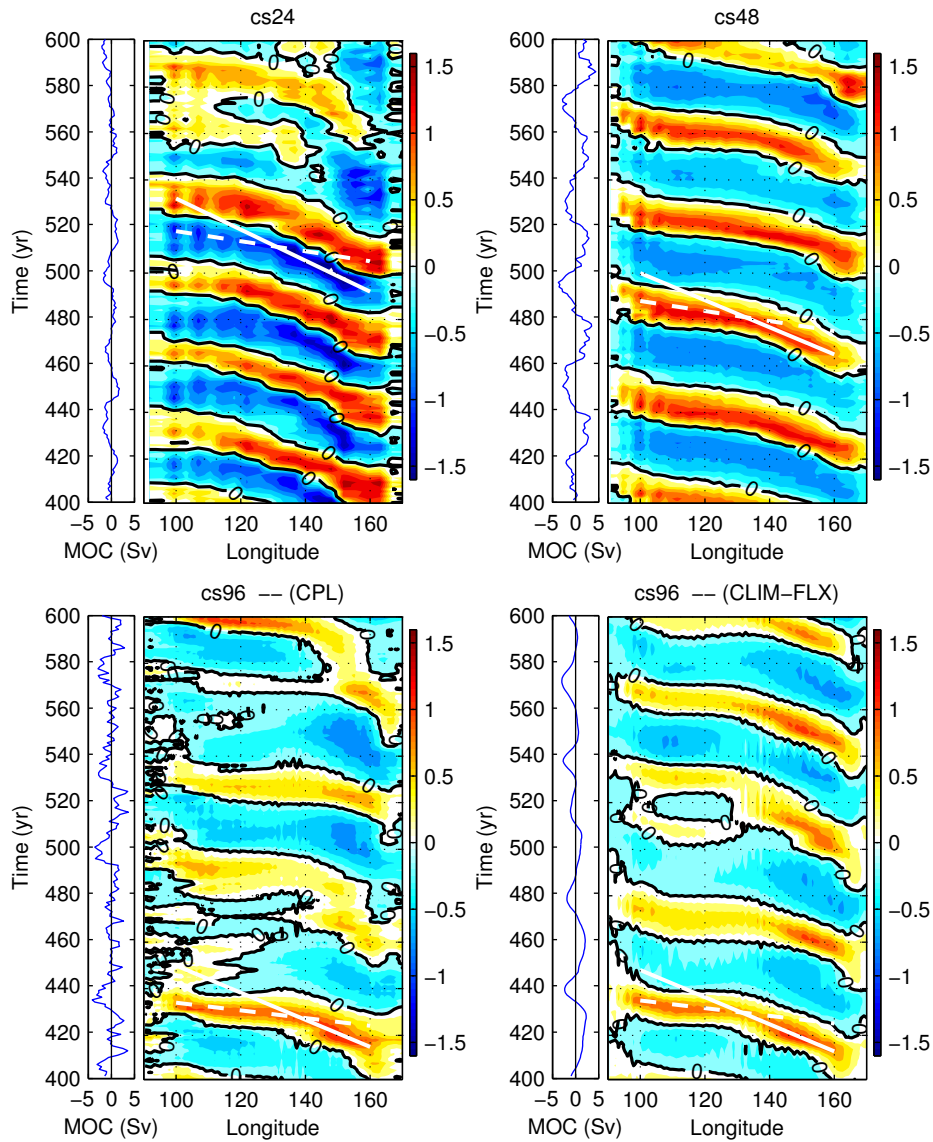


**Fig. 7** Hovmöller diagrams of yearly potential temperature anomalies in the thermocline (in K) for the last 200 yr of simulation for coupled runs cs24 (top left), cs48 (top right), cs96 (bottom left) and the forced run CLIM-FLX of cs96 (bottom right). The east-west cross section is computed between  $55^{\circ}$ - $65^{\circ}$ N,  $60^{\circ}$ - $70^{\circ}$ N and  $65^{\circ}$ - $75^{\circ}$ N for cs24, cs48 and for both cs96 runs respectively, and at the depth of the maximum anomalies, i.e. 265 m for cs24 and 540 m for cs48 and cs96 runs. The zero contour is thick black line. Continuous (dashed) white lines show an estimate of the westward phase velocity of temperature anomalies across the eastern (western) half of the small basin. The corresponding MOC index is shown on the left of each diagram

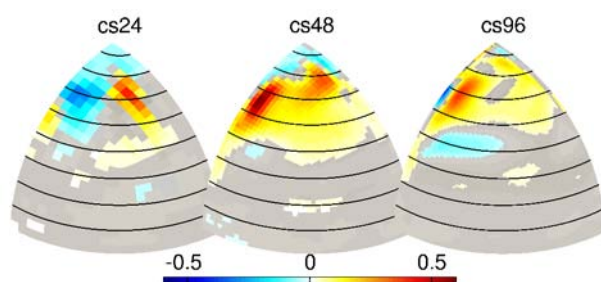


**Fig. 8** Yearly Sea Surface Temperature (SST) anomalies (K) associated with one standard deviation of the yearly MOC index at lag=0, for cs24 (left), cs48 (centre) and cs96 (right). Regions that are not statistically significant at the 5% level are grey shaded. The thin black contours mark latitude circles every  $10^\circ$  from  $10^\circ\text{N}$  to  $80^\circ\text{N}$

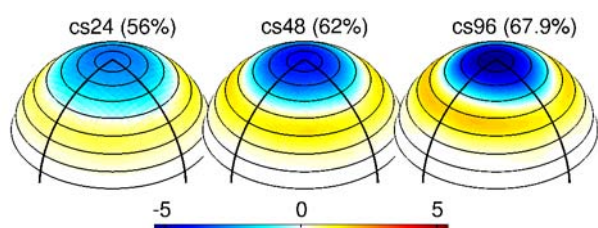


**Fig. 9** First EOF of the yearly Sea Level Pressure Anomaly (SLPA, in hPa) in the northern hemisphere. The explained variance is displayed at the top of each plots. The EOFs are normalized by the standard deviation of their corresponding PC. The thin black contours mark latitude circles every  $10^\circ$  from  $10^\circ\text{N}$  to  $80^\circ\text{N}$ , and the thick orthogonal black lines the boundaries of the small basin

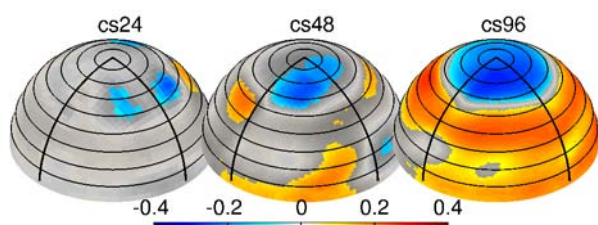


**Fig. 10** Correlation between yearly Sea Level Pressure and the yearly MOC index 2 yr later (i.e. when the most significant correlations are found). Regions that are not statistically significant at the 5% level are grey shaded. The thin black contours mark latitude circles every  $10^\circ$  from  $10^\circ\text{N}$  to  $80^\circ\text{N}$ , and the thick orthogonal black lines the boundaries of the small basin

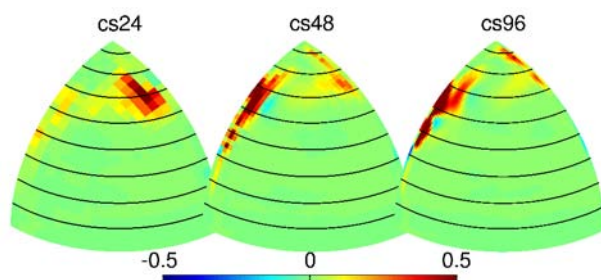


**Fig. 11** Term  $-\overline{u'T'\nabla T}$  related to baroclinic instability eddy fluxes in the potential temperature variance budget averaged over the upper 1000 m ocean and over several MOC oscillation periods, in  $\text{K}^2 \text{yr}^{-1}$ . The thin black contours mark latitude circles every  $10^\circ$  from  $10^\circ\text{N}$  to  $80^\circ\text{N}$

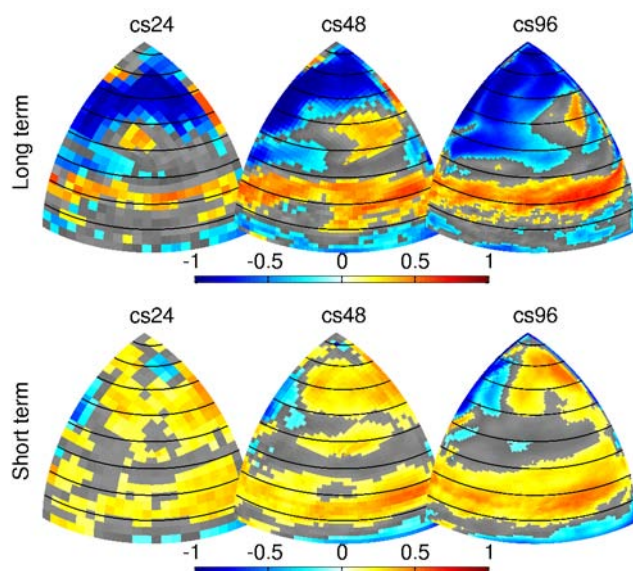


**Fig. 12** Correlation between Sea Surface Temperature (SST) anomalies and the ocean-atmosphere heat fluxes ( $Q$ , positive downward for a release of heat into the ocean) for the multidecadal signal - 10 yr running mean - (top) and interannual signal - residual variability of the 10 yr running mean - (bottom). Regions that are not statistically significant at the 5% level are grey shaded. The thin black contours mark latitude circles every  $10^\circ$  from  $10^\circ\text{N}$  to  $80^\circ\text{N}$

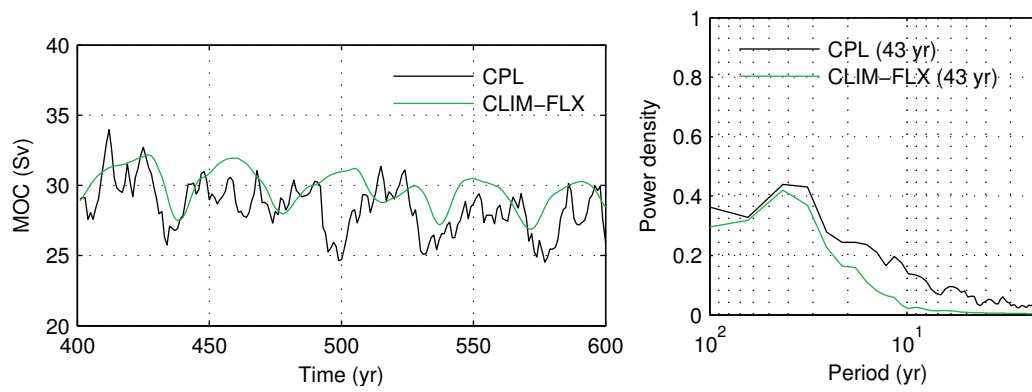


**Fig. 13** Yearly MOC time series (left) and respective power spectra (right) for the coupled configuration (CPL, black) and the ocean-only configuration forced by climatological fluxes and SST restoring toward climatological values (CLIM-FLX, green) for cs96. The time scale of the dominant period of each time series is displayed on the right panel, the difference with Fig. 3 results from the shorter time series used for the spectrum